

Article

Introducing CuCo₂S₄ Nanoparticles on Reduced Graphene Oxide for High-Performance Supercapacitor

Xue Fang¹, Cong Yang², Xiaochen Zhang¹, Yang Wang¹ and Jiali Yu^{2,*}

¹ Institute of Advanced Technology, Heilongjiang Academy of Sciences, Harbin 150001, China; xiaoxue@iathas.ac.cn (X.F.); xiaochen@iathas.ac.cn (X.Z.); wangyang@iathas.ac.cn (Y.W.)

² Institute of Low-dimensional Materials Genome Initiative, College of Chemistry and Environmental Engineering, Shenzhen University, Shenzhen 518060, China; yang@iathas.ac.cn

* Correspondence: jialiyu@szu.edu.cn

Abstract: In this work, a bimetallic sulfide-coupled graphene hybrid was designed and constructed for capacitive energy storage. The hybrid structure involved decorating copper–cobalt–sulfide (CuCo₂S₄) nanoparticles onto graphene layers, with the nanoparticles anchored within the graphene layers, forming a hybrid energy storage system. In this hybrid structure, rGO can work as the substrate and current collector to support the uniform distribution of the nanoparticles and provides efficient transportation of electrons into and out of the electrode. In the meantime, CuCo₂S₄-active materials are expected to offer an evident enhancement in electrochemical activities, due to the rich valence change provided by Cu and Co. Benefiting from the integrated structure of CuCo₂S₄ nanoparticles and highly conductive graphene substrates, the prepared CuCo₂S₄@rGO electrode exhibited a favorable capacitive performance in 1 M KOH. At 1 A g^{−1}, CuCo₂S₄@rGO achieved a specific capacitance of 410 F g^{−1}. The capacitance retention at 8 A g^{−1} was 70% of that observed at 1 A g^{−1}, affirming the material's excellent rate capability. At the current density of 5 A g^{−1}, the electrode underwent 10,000 charge–discharge cycles, retaining 98% of its initial capacity, which indicates minimal capacity decay and showcasing excellent cycling performance.

Keywords: graphene oxides; metallic sulfides; CuCo₂S₄ nanoparticles; supercapacitor; composites



Citation: Fang, X.; Yang, C.; Zhang, X.; Wang, Y.; Yu, J. Introducing CuCo₂S₄ Nanoparticles on Reduced Graphene Oxide for High-Performance Supercapacitor. *Nanomaterials* **2024**, *14*, 182. <https://doi.org/10.3390/nano14020182>

Academic Editor: Fabrizio Pirri

Received: 7 December 2023

Revised: 20 December 2023

Accepted: 22 December 2023

Published: 12 January 2024



Copyright: © 2024 by the authors. Licensee MDPI, Basel, Switzerland. This article is an open access article distributed under the terms and conditions of the Creative Commons Attribution (CC BY) license (<https://creativecommons.org/licenses/by/4.0/>).

1. Introduction

Over recent decades, supercapacitors (SCs) have garnered significant attention as a dependable electrochemical energy storage (EES) system due to their extended lifespan and high power density. The advent of pseudocapacitors, originally introduced by Conway, has spurred extensive investigation owing to their rapid and reversible faradic reactions occurring at the surface [1–3]. Lately, scientists have focused on exploring the synthesis of bimetallic compounds using various transition metal elements such as Co, Ni, Fe, Mn, Mo, and so on for supercapacitor applications. Particularly, Manickam Minakshi et al. fabricated Nano α -NiMoO₄ and CoMoO₄ as new active materials for electrochemical supercapacitors, which demonstrated excellent energy storage performances [4–6]. In addition to binary metal oxides, binary metal sulfides have shown remarkable properties such as enhanced electrical conductivity, increased redox sites, and expansive oxidation states resulting from the synergistic combination of two metal sulfides within a single molecule [7,8]. To date, several binary transition metal sulfides, including NiCo₂S₄, MnCo₂S₄, CuCo₂S₄, ZnCo₂S₄, and FeCo₂S₄, have found successful applications in the realm of SCs [9–11]. Notably, compared to other transition metal compounds, CuCo₂S₄, initially synthesized by Ye et al., is considered to be one of the most promising electrode materials due to its environmental friendliness and the low cost of Cu. By replacing the oxygen atom in CuCo₂O₄ with sulfur atoms, CuCo₂S₄ can be obtained with the well-preserved spinel structure of the original compound. CuCo₂S₄ exhibits enhanced electron transport due to its higher electronegativity and smaller bandgap as compared with CuCo₂O₄. This

superior electron transport capability is believed to positively impact on the electrochemical performance. As a result, CuCo_2S_4 nanoparticles synthesized by Chen et al. through a hydrothermal process exhibited a specific capacity of 90.6 mAh g^{-1} at a current density of 2 A g^{-1} . Impressively, these nanoparticles retained 47.9% of their capacity when the current density was increased from 2 to 50 A g^{-1} . However, challenges persist with CuCo_2S_4 electrodes, primarily stemming from issues such as self-agglomeration and poor conductivity, leading to limitations in the rate capability and cycle stability [12–14].

To address this challenge, the strategic amalgamation of CuCo_2S_4 with a highly conductive carbon matrix becomes imperative. Fortunately, graphene emerges as an optimal candidate owing to its exceptional conductivity and expansive surface area. When graphene is combined with inorganic materials such as metal oxides/hydroxides/sulfides, unique structural features and synergistic electrochemical properties can be imparted to the resulting graphene-based nanohybrids [15–18]. In fact, various functional nanohybrids comprising metal oxides or hydroxides have been successfully constructed to achieve a higher pseudocapacitance and enhanced electrochemical performance. Moreover, based on prior findings, the penetration depth of electrolyte ions into the electrode material is approximately 20 nm. Hence, reasonably reducing the size of active materials is a desired approach [19–21].

Inspired by prior works, we fabricated the $\text{CuCo}_2\text{S}_4@\text{rGO}$ composite electrode using a straightforward two-step solvothermal approach in this study. The incorporation of CuCo_2S_4 nanoparticles is expected to offer an evident enhancement in electrochemical activities, due to the rich valence change provided by Cu and Co. Simultaneously, reduced graphene oxide (rGO) plays a multifaceted role: providing nucleation sites for CuCo_2S_4 growth, preventing the agglomeration of CuCo_2S_4 nanoparticles, and serving as a conductive scaffold, thereby amplifying the conductivity of $\text{CuCo}_2\text{S}_4@\text{rGO}$. Furthermore, by depositing the $\text{CuCo}_2\text{S}_4/\text{rGO}$ composite onto nickel foam, the resultant product can function as a freestanding supercapacitor electrode for energy storage purposes. Benefiting from the integrated structure of CuCo_2S_4 nanoparticles and highly conductive graphene substrates, the prepared CuCo_2S_4 electrode exhibited a favorable capacitive performance in 1 M KOH. At 1 A g^{-1} , $\text{CuCo}_2\text{S}_4@\text{rGO}$ achieved a specific capacitance of 410 F g^{-1} . The capacitance retention at 8 A g^{-1} was 70% of that observed at 1 A g^{-1} , affirming the material's excellent rate capability. At the current density of 5 A g^{-1} , the electrode underwent 10,000 charge–discharge cycles, retaining 98% of its initial capacity, which indicates minimal capacity decay and showcasing excellent cycling performance.

2. Experimental Section

2.1. Preparation of $\text{CuCo}_2\text{O}_4@\text{rGO}$

An amount of 15 mg of GO powder (Zhongke, Shanghai, China) was dispersed in 5 mL of deionized (DI) water, forming a 3 mg mL^{-1} GO aqueous dispersion. Then, 15 mL of a 1:1 mixture of DI water and ethanol was added into the GO dispersion, labeled as solution A. Amounts of 483.2 mg of $\text{Cu}(\text{NO}_3)_2$ and 582.1 mg of $\text{Co}(\text{NO}_3)_2$ were dispersed in 10 mL of DI water, labeled as solution B.

Solution A was slowly dripped into solution B while stirring continuously for 2 h. Then, the resulting mixture was transferred into a polytetrafluoroethylene reaction vessel and a hydrothermal reaction was conducted at $160 \text{ }^\circ\text{C}$ for 6 h. After the reaction, the obtained black sample was filtered, washed, and dried. Finally, the sample was annealed at $500 \text{ }^\circ\text{C}$ for 1 h in a tube furnace to enhance the crystallinity of the sample. This product is denoted as $\text{CuCo}_2\text{O}_4@\text{rGO}$.

2.2. Preparation of $\text{CuCo}_2\text{S}_4@\text{rGO}$

Amounts of 25 mg of the aforementioned $\text{CuCo}_2\text{S}_4@\text{rGO}$ sample, along with 100 mg of TAA, were added into 30 mL of anhydrous ethanol to form a homogeneous dispersion. This mixture was then transferred into a polytetrafluoroethylene reaction vessel and a hydrothermal reaction was conducted at $180 \text{ }^\circ\text{C}$ for 6 h.

After the reaction, the resulting product was washed 5 times with DI water and then vacuum-dried to obtain the CuCo₂S₄@rGO sample.

2.3. Preparation of CuCo₂S₄@rGO@nickel Foam Freestanding Electrode

A commercial nickel foam material was selected as the electrode substrate, and a slurry of CuCo₂S₄@rGO material was prepared following a specific method. The slurry was uniformly applied onto the nickel foam substrate using a blade-coating method, creating a highly flexible nickel foam-based electrode. The slurry preparation method is outlined as follows:

The nickel foam was cut into rectangular pieces measuring 1 cm × 3 cm, then subjected to ultra-sonication in water and ethanol for 30 min, respectively, to remove the surface impurities, followed by overnight vacuum-drying.

A specific amount of polyvinylidene fluoride (PVDF) was put into a mortar with a small amount of NMP (N-methyl-2-pyrrolidone), and ground until the PVDF was completely dissolved. Then, a specific amount of conductive carbon black (acetylene black) and CuCo₂S₄@rGO was added into the PVDF, continuing to grind until a uniform, relatively viscous black slurry was formed.

Due to the hygroscopic nature of PVDF, all materials and tools need to be moisture-free. Pre-dissolving PVDF in an NMP solution prevents it from coagulating due to air humidity. The mass ratio of the slurry comprises PVDF (binder), conductive agent (acetylene black), and electrode-active material in a ratio of 1:1:8. The addition of NMP is empirical, typically within a range of approximately 5 to 10 drops, which may be adjusted according to the specific materials used.

Finally, the slurry is blade-coated onto the front 1 cm × 1 cm area of the foam nickel. An average coating is achieved by using a syringe needle to evenly distribute the slurry. The electrode is then placed in a vacuum oven and dried at 80 °C overnight.

2.4. Measurements

The phase constituents and crystal structure of the specimens were analyzed using powder X-ray diffractometry (XRD) conducted on a MiniFlex600 instrument from Rigaku, Tokyo, Japan. The measurements were performed at 40 kV and 15 mA with nickel-filtered Cu-K α radiation over an angular range spanning from 3° to 80°, at a scanning rate of 5° per minute. To characterize the morphology and structure of the samples, field-emission scanning electron microscopy (FESEM) was conducted using a JSM-7800F instrument (Tokyo, Japan), while transmission electron microscopy (TEM) analysis was carried out using a JEM2100 instrument (Tokyo, Japan). Additionally, X-ray photoelectron spectroscopy (XPS) measurements were conducted utilizing an Escalab-250Xi electron spectrometer manufactured by Thermo Scientific (Waltham, MA, USA), with Al-K α radiation employed as the X-ray source.

The electrochemical characteristics of CuCo₂S₄@rGO, employed as the working electrode, were examined within a three-electrode cell containing a 3 M KOH aqueous solution. Platinum plate and Hg/HgO were utilized as the counter and reference electrodes, respectively, while the mass of CuCo₂S₄@rGO stood at 2.0 mg. Various electrochemical techniques including cyclic voltammetry (CV), galvanostatic charge–discharge (GCD), and electrochemical impedance spectroscopy (EIS) were performed to assess its electrochemical performance using an electrochemical workstation (Yicheng Hengda Technology Co., Ltd., Beijing, China). Deriving from the galvanostatic discharge curve, the specific capacitance (C_s) was calculated utilizing the following equation:

$$C_s = \frac{I\Delta t}{m\Delta V} \quad (1)$$

Here, I (A) represents the steady discharge current, while m (g) stands for the weight of the active material within the electrode. Δt (s) denotes the constant discharge duration, and ΔV (V) signifies the potential window utilized [22].

3. Results and Discussion

The $\text{CuCo}_2\text{O}_4@\text{rGO}$ sample, obtained after the initial annealing step, was examined using field-emission scanning electron microscopy (SEM), as depicted in Figure 1a,b. The observations revealed a morphology of plenty of nanoparticles encapsulated within the graphene layers. From the subsequent transmission electron microscopy (TEM) investigation (Figure 1c–e), it can be seen that the distributions of the nanoparticles are very uniform across the whole thin graphene layers. The nanoparticles demonstrate an irregular flake morphology with a lateral size range of 10~30 nm.

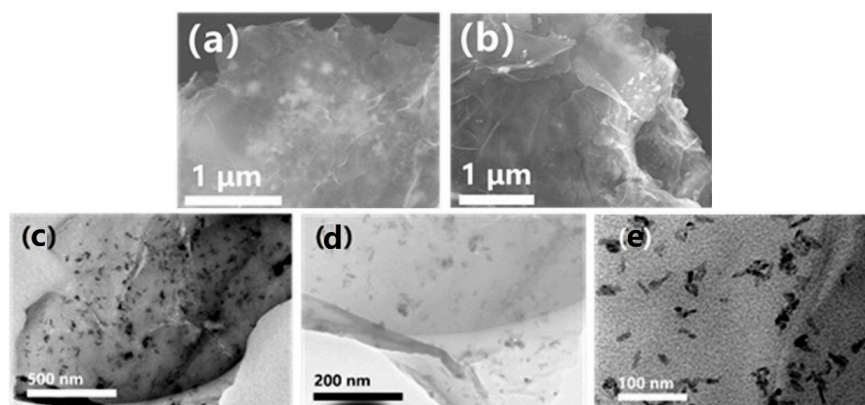


Figure 1. (a,b) FESEM images of $\text{CuCo}_2\text{O}_4@\text{rGO}$ sample. (c–e) TEM images of $\text{CuCo}_2\text{O}_4@\text{rGO}$ sample.

The sulfidation process took place within a hydrothermal reactor, utilizing thioacetamide (TAA) as the sulfur source and anhydrous ethanol as the solvent. During the hydrothermal process, the GO is further reduced during the solvothermal process due to the reducibility of S^{2-} derived from TAA, resulting in enhanced electrical conductivity. Then, the copper cobalt oxides were decomposed as the temperature rose and transformed into CuCo_2S_4 nanoparticles, finally anchoring on the rGO. The reaction proceeded at a temperature of 180 °C for 6 h, resulting in the formation of uniformly distributed particulate CuCo_2S_4 on the graphene sheets, as depicted in Figure 2. The particles exhibited uniform diameters and were evenly dispersed within the graphene layers. Through TEM analysis, the sample morphologies were examined. As depicted in Figure 2c,d, nanoscale sulfide particles with diameters ranging from 5 to 10 nm can be observed, which are uniformly anchored within the layers of oxidized graphene. Graphene encapsulated the nanoparticles, displaying a homogeneously stable morphology. Since graphene possesses excellent electronic conductivity, the close contact between the nanoparticle and graphene could provide expedited pathways for electron transport and facilitate energy storage kinetics. The clearly visible lattice fringes, exhibiting lattice spacings of 0.55 nm and 0.33 nm, correspond to the (111) and (200) crystal planes of cubic CuCo_2S_4 , respectively.

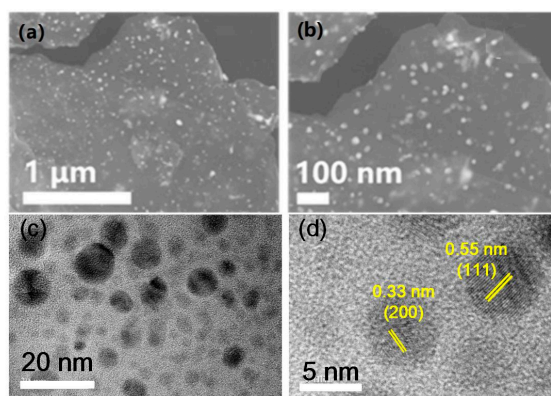


Figure 2. (a,b) SEM images of $\text{CuCo}_2\text{S}_4@\text{rGO}$ sample; (c,d) TEM images of $\text{CuCo}_2\text{S}_4@\text{rGO}$ sample.

The X-ray diffraction (XRD) analysis of the samples revealed distinctive patterns. Figure 3a represents the XRD spectrum of $\text{CuCo}_2\text{O}_4@\text{rGO}$. By comparing the sample's XRD peaks with the standard PDF cards, we identified the predominant presence of CuCo_2O_4 , corresponding to the JCPDS 001-1155 [23] standard card.

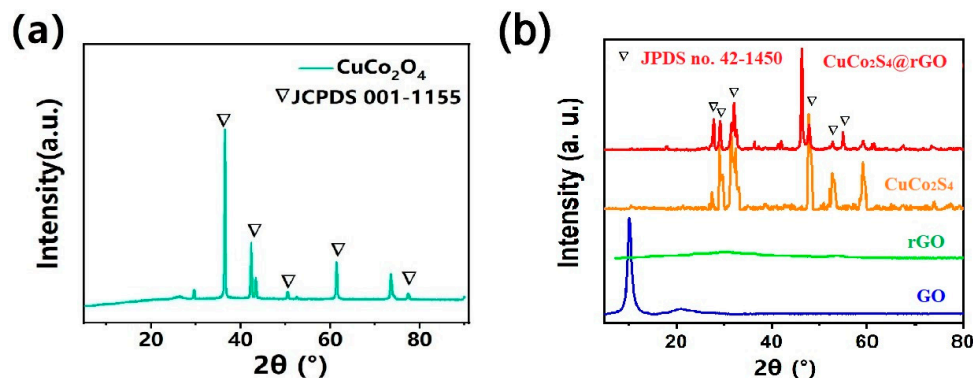


Figure 3. (a) XRD patterns of $\text{CuCo}_2\text{O}_4@\text{rGO}$; (b) XRD patterns of GO, rGO, CuCo_2S_4 , and $\text{CuCo}_2\text{S}_4@\text{rGO}$.

After sulfuration, as shown in Figure 3b, the crystalline structure of $\text{CuCo}_2\text{S}_4@\text{rGO}$ is identified by the XRD technique. The diffraction peaks can be assigned to the cubic phase of spinel CuCo_2S_4 based on JCPDS No.42–1450 [24], respectively. Moreover, the low peak intensity and other peaks that appeared between 15° and 90° indicate the poor crystallization and impurity of CuCo_2S_4 [25]. On the base of the XRD patterns, the crystalline structure model of CuCo_2S_4 is revealed in Figure 3b.

Figure 4 presents the Raman spectra of the $\text{CuCo}_2\text{S}_4@\text{rGO}$ sample. For comparison, the Raman spectra of graphene oxide (GO) that was used as the precursor for preparing the rGO in the $\text{CuCo}_2\text{S}_4@\text{rGO}$ sample is also provided. Notably, the characteristic peaks corresponding to defect (D) and graphite (G) carbons were observed in both of the two samples at approximately 1350 cm^{-1} and 1580 cm^{-1} wavenumbers, respectively. The I_D/I_G ratio of pristine GO is 0.89. While after the hydrothermal process, the I_D/I_G ratio for the $\text{CuCo}_2\text{S}_4@\text{rGO}$ sample decreased to 0.72, indicating an increment in graphitization in the material. This enhancement promotes better electron conduction within the graphene layers [26]. Interestingly, the Raman spectrum of the $\text{CuCo}_2\text{S}_4@\text{rGO}$ sample did not exhibit distinct peaks attributable to the embedded metal sulfides. This absence may stem from either the relatively low content of metal sulfides or the low intensity of the diffraction peaks.

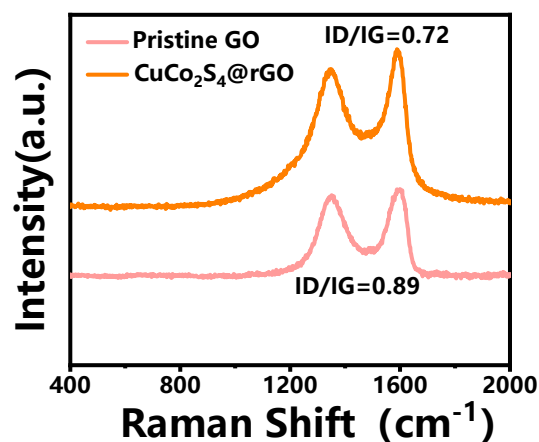


Figure 4. Raman spectra of $\text{CuCo}_2\text{S}_4@\text{rGO}$ sample and pristine GO.

By applying X-ray photoelectron spectroscopy (XPS) to analyze the surface chemical information of the $\text{CuCo}_2\text{S}_4@\text{rGO}$ sample (Figure 5), the broad scan spectrum indicates the

presence of six primary elements, S, C, N, O, Co, and Cu, in the sample. The atomic ratios of the different elements are listed in Table 1.

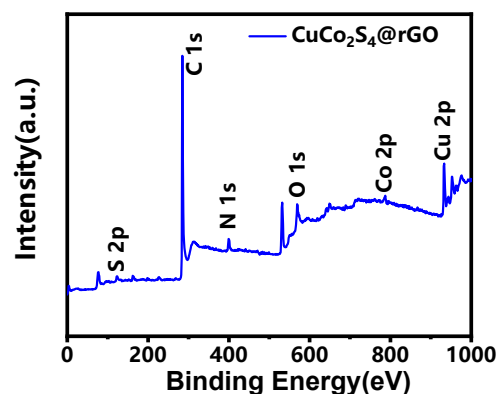


Figure 5. XPS broad scan of $\text{CuCo}_2\text{S}_4@\text{rGO}$ samples.

Table 1. Atomic percentages of the elements in XPS analysis.

Element	Atomic %
C	77.99
O	11.08
N	4.29
Co	1.68
Cu	3.40
S	1.56

By deconvoluting the fine spectra of Cu 2p, Co 2p, C 1s, and S 2p, the chemical composition and electronic bonding states of the elements were analyzed. The high-resolution XPS spectrum of Cu 2p (Figure 6a) demonstrates Cu 2p_{3/2} and Cu 2p_{1/2} peaks along with two satellite peaks (marked as “sat”). Cu 2p_{3/2} and Cu 2p_{1/2} can be further divided into two spin–orbit doublets, indicating the coexistence of Cu⁺ and Cu²⁺. The Cu⁺ peaks of Cu 2p_{1/2} and Cu 2p_{3/2} were identified at 952.6 eV and 932.75 eV, respectively, with a splitting energy of 19.85 eV. Additionally, two dominant peaks corresponding to Cu²⁺ were resolved at 935.94 eV and 955.92 eV. The Co 2p spectrum (Figure 6b) displayed two peaks at the binding energies of near 781 eV and 797 eV, corresponding to Co 2p_{3/2} and Co 2p_{1/2}, respectively, which is consistent with the literature [27]. Co 2p_{3/2} and Co 2p_{1/2} can be further split into two spin–orbit lines, evidencing the presence of divalent and trivalent Co species. Figure 6c represents the C 1s fine spectrum, revealing deconvoluted peaks attributed to C–C, C–O, and C=O bonds [28]. The deconvoluted peaks of the S 2p spectrum exhibited two primary peaks centered at 161.8 eV and 163.1 eV, which are the characteristic peaks of metal sulfides, corresponding to sulfides and disulfides, respectively [29]. Additionally, a significant peak around 165 eV corresponding to C–S–C bonds can be observed, indicating the bonding between sulfides and graphene layers. The weak SO_x peak near 169.5 eV represents a low sulfur content in the oxide, which is due to the shortcomings of the liquid-phase hydrothermal sulfidation method [30]. The XPS results confirm the successful construction of a well-defined binary metal sulfide stably bonded on the reduced graphene oxide layers. Since the binary metal sulfide is highly active for electrochemical reactions and the rGO is conductive, the combination of these two materials could provide a synergic effect for energy storage. At first, rGO can work as the substrate and the current collector supports the uniform distribution of the nanoparticles and provides the efficient transportation of electrons into and out of the electrode. Secondly, CuCo_2S_4 -active materials are expected to offer an evident enhancement in electrochemical activities, due to the rich valence change provided by Cu and Co. As a result, a high specific capacitance and rate performance were achieved by the as-synthesized $\text{CuCo}_2\text{S}_4@\text{rGO}$.

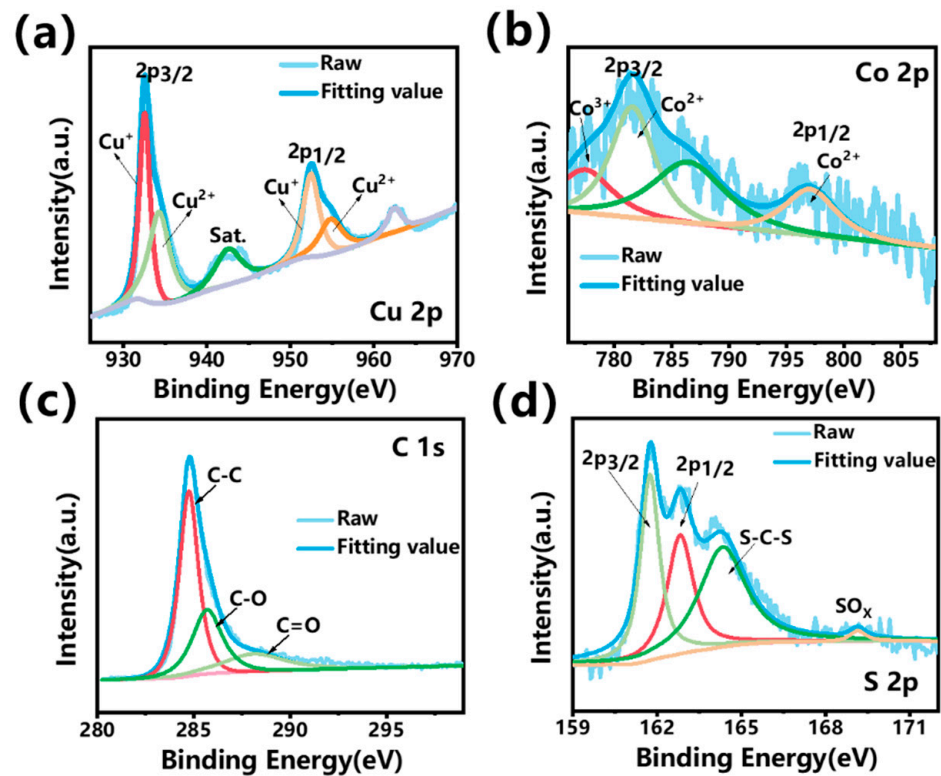
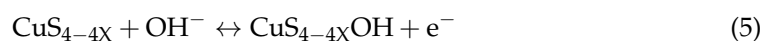
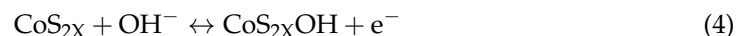
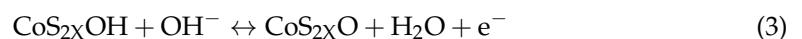


Figure 6. High-resolution XPS spectra of $\text{CuCo}_2\text{S}_4@\text{rGO}$ samples: (a) Cu 2p; (b) Co 2p; (c) C 1s; (d) S 2p.

The electrochemical performances of the $\text{CuCo}_2\text{S}_4@\text{rGO}$ sample were evaluated in a three-electrode system with 1 M KOH aqueous solution as the electrolyte, Hg/HgO as the reference electrode, and Pt as the counter electrode. For the convenience of testing, $\text{CuCo}_2\text{S}_4@\text{rGO}$ was loaded on a nickel foam as a freestanding electrode. Figure 7a shows the cyclic voltammetry (CV) curves of $\text{CuCo}_2\text{S}_4@\text{rGO}$ at scan rates ranging from 5 to 100 mV s^{-1} within a potential window of 0~0.8 V. It can be seen from Figure 7a that a pair of broad redox peaks can be clearly observed in all the CV curves, indicating that the capacitances are mainly derived from the pseudocapacitance associated with the reversible faradic reactions of the metal sulfide [31,32]. Furthermore, a minor shift in the peak current position can be observed with the increasing scan rates, attributed to the polarization phenomenon. At the scan rate of 100 mV s^{-1} , the CV maintained its shape observed at lower scan rates, verifying the superior kinetic reversibility and rate performance of the sample. The observed redox peaks are attributable to reversible faradaic reactions, as depicted by the following equations:



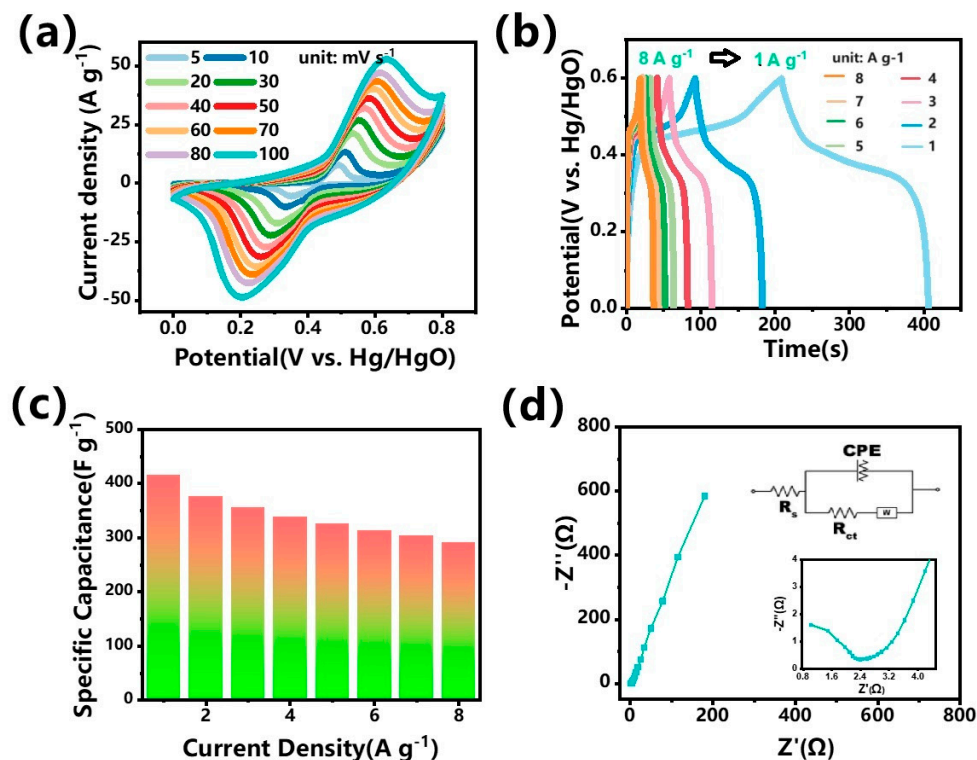


Figure 7. Electrochemical performance of $\text{CuCo}_2\text{S}_4@\text{rGO}$ as supercapacitor electrode in the three-electrode cell: (a) CV curves of $\text{CuCo}_2\text{S}_4@\text{rGO}$ at different scan rate; (b) GCD curves of $\text{CuCo}_2\text{S}_4@\text{rGO}$ at different current density; (c) gravimetric specific capacitance values of $\text{CuCo}_2\text{S}_4@\text{rGO}$ based on GCD curves; (d) Nyquist plot of the $\text{CuCo}_2\text{S}_4@\text{rGO}$ electrode; the inset shows the equivalent circuit.

The GCD curves at the current densities ranging from 1 A g^{-1} to 8 A g^{-1} reveal symmetric shapes with almost equivalent charge–discharge durations, manifesting the good columbic efficiency of the sample (Figure 7b). Moreover, it should be noted that as the current density increases, no visible IR drops can be observed in the curves obtained at high current densities, indicating the excellent conductivity of $\text{CuCo}_2\text{S}_4@\text{rGO}$, which is meaningful for the high rate performance. In fact, from the electrode impedance spectroscopy (EIS) results of the sample, the R_s and R_{ct} of the sample is only about 0.85Ω and 1.55Ω , respectively (Figure 7d). The calculated specific capacitance based on the GCD curves is presented in Figure 7c. At current densities of 1 A g^{-1} , 2 A g^{-1} , 3 A g^{-1} , 4 A g^{-1} , 5 A g^{-1} , 6 A g^{-1} , 7 A g^{-1} , and 8 A g^{-1} , the specific capacities were 415 F g^{-1} , 376 F g^{-1} , 355 F g^{-1} , 338 F g^{-1} , 325 F g^{-1} , 313 F g^{-1} , 303 F g^{-1} , and 290 F g^{-1} , respectively. The capacitance retention at 8 A g^{-1} was 70% of that observed at 1 A g^{-1} , affirming the material’s excellent rate capability [33]. The results demonstrated above manifest that the conductivity and pseudocapacitive performance provided by the rGO substrate and uniformly distributed CuCo_2S_4 nanoparticles are favorable for the fast diffusion of electrolyte ion and electron transportations during electrochemical reactions, thus leading to a higher electrochemical activity and energy storage performance.

Figure 8 displays the cyclic performance of $\text{CuCo}_2\text{S}_4@\text{rGO}$ in the three-electrode system, demonstrating exceptional cycling stability. At the current density of 5 A g^{-1} , the electrode underwent 10,000 charge–discharge cycles, retaining 98% of its initial capacity, which indicates minimal capacity decay and showcasing excellent cycling performance.

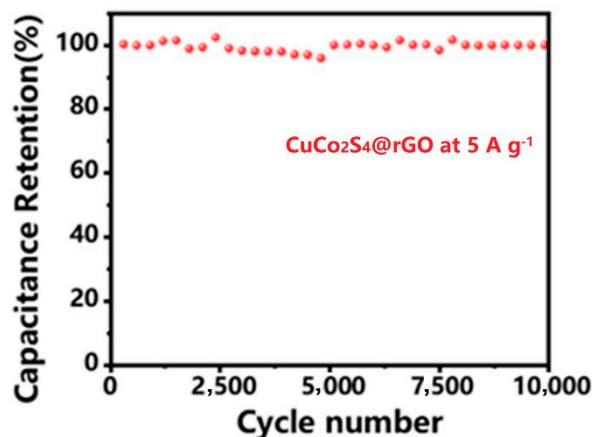


Figure 8. Cycle performance of $\text{CuCo}_2\text{S}_4@\text{rGO}$ as supercapacitor electrode in the three-electrode measurement.

Table 2 illustrates the comparison of the energy storage performance obtained in our work with other recently reported sulfide–graphene composite nanomaterials [34]. As can be observed, the specific capacitance reported in this work is comparable to or exceeds many of the existing counterpart works, although the comparative analysis indicates that the specific capacitance achieved in this study is superior. However, there is still room for optimization to further increase the energy storage of $\text{CuCo}_2\text{S}_4@\text{rGO}$. The optimization techniques include modifying the morphologies of CuCo_2S_4 and the loading densities of CuCo_2S_4 , which will be explored in our future work.

Table 2. Comparison of the energy storage performance of electrode based on transition metal sulfide composited with graphene.

Electrode	Electrolyte	Scan Rate/Current Density	Specific Capacitance	Reference
$(\text{Ni},\text{Mo})\text{S}_2/\text{G}$	2 M KOH	1 A g^{-1}	376 F g^{-1}	[28]
$\text{Co}_3\text{S}_4/\text{CoMo}_2\text{S}_4$ (CMS)-rGO	6 M KOH	1 A g^{-1}	457.8 F g^{-1}	[29]
NiS/GO	3 M KOH	1 A g^{-1}	400 F g^{-1}	[31]
$\text{CuCo}_2\text{S}_4@\text{rGO}$	1 M KOH	1 A g^{-1}	415 F g^{-1}	This work

The excellent electrochemical performance observed in the $\text{CuCo}_2\text{S}_4@\text{rGO}$ electrode can be attributed to several key factors. Firstly, reduced graphene oxides serve as a conductive matrix and scaffold for CuCo_2S_4 deposition. This role facilitates electron transport and prevents CuCo_2S_4 agglomeration, thus enhancing electrode material utilization and rate capability. Secondly, the presence of CuCo_2S_4 nanoparticles effectively reduces the distance for ion transmission and provides ample active sites for faradaic redox reactions, thereby amplifying the electrochemical performance. Thirdly, the direct growth of CuCo_2S_4 nanoparticles on rGO mitigates the stress induced during cycling, thereby bolstering the stability of CuCo_2S_4 within the electrode system.

4. Conclusions

In this work, we decorated rGO with pseudocapacitive active CuCo_2S_4 nanoparticles to address the issues of the poor cyclic performance and low rate capability observed in pseudocapacitive materials. Employing a hydrothermal synthesis method, $\text{CuCo}_2\text{S}_4@\text{rGO}$ composites were successfully synthesized, followed by low-temperature annealing to enhance the crystallinity of the metal oxides. Subsequently, utilizing TAA as a sulfur source, a hydrothermal sulfidation process successfully yielded $\text{CuCo}_2\text{S}_4@\text{rGO}$ nanocomposites. The results indicate the superior performance of the $\text{CuCo}_2\text{S}_4@\text{rGO}$ sample. In a 1 M KOH electrolyte, at 1 A g^{-1} , $\text{CuCo}_2\text{S}_4@\text{rGO}$ achieved a specific capacitance of 410 F g^{-1} .

The capacitance retention at 8 A g⁻¹ was 70% of that observed at 1 A g⁻¹, affirming the material's excellent rate capability. At the current density of 5 A g⁻¹, the electrode underwent 10,000 charge–discharge cycles, retaining 98% of its initial capacity, which indicates minimal capacity decay and showcasing an excellent cycling performance.

Author Contributions: Conceptualization, J.Y. and X.F.; methodology, C.Y. and J.Y.; validation, X.F., C.Y. and J.Y.; formal analysis, X.F., C.Y. and J.Y.; investigation, X.F., C.Y. and J.Y.; resources, J.Y., Y.W. and X.Z.; data curation, X.F. and J.Y.; writing—original draft preparation, X.F., C.Y. and J.Y.; writing—review and editing, X.F. and J.Y.; supervision, Y.W. and J.Y.; funding acquisition, J.Y. and X.F. All authors have read and agreed to the published version of the manuscript.

Funding: This work was supported by the Guangdong Basic and Applied Basic Research Foundation (2022A1515011507), University Stability Support plan of Shenzhen (20220805094705001), and the Program for Guangdong Introducing Innovative and Entrepreneurial Teams (2019ZT08C642). Heilongjiang Provincial Institutes Basic Scientific Research Business Funds.

Informed Consent Statement: Not applicable.

Data Availability Statement: The raw data will be available from the corresponding author upon reasonable request.

Conflicts of Interest: The authors declare no conflict of interest.

References

1. Guan, C.; Liu, X.; Elshahawy, A.M. Metal-organic framework derived hollow CoS₂ nanotube arrays: An efficient bifunctional electrocatalyst for overall water splitting. *Nanoscale Horiz.* **2017**, *2*, 342–348. [[CrossRef](#)] [[PubMed](#)]
2. Lei, X.; Ge, S.; Tan, Y. High capacity and energy density of Zn-Ni-Co-P nanowire arrays as an advanced electrode for aqueous asymmetric supercapacitor. *ACS Appl. Mater. Interfaces* **2020**, *12*, 9158–9168. [[CrossRef](#)] [[PubMed](#)]
3. Yang, J.; Yu, C.; Fan, X. Electroactive edge site-enriched nickel-cobalt sulfide into graphene frameworks for high-performance asymmetric supercapacitors. *Energy Environ. Sci.* **2016**, *9*, 1299–1307. [[CrossRef](#)]
4. Baskar, S.; Kalimuthu, V.S.; Ramakrishnan, K.S. Nano a-NiMoO₄ as a new electrode for electrochemical supercapacitors. *RSC Adv.* **2013**, *3*, 352–357.
5. Ramya, R.; Manickam, M. Fabrication of ultrathin CoMoO₄ nanosheet modified with chitosan and their improved performance in energy storage device. *RSC Adv.* **2015**, *44*, 6158–6168.
6. Barmi, M.J.; Minakshi, M. Tuning the redox properties of the nanostructured CoMoO₄ electrode: Effects of surfactant content and synthesis temperature. *Chem. Eur. J.* **2016**, *81*, 964–977. [[CrossRef](#)]
7. Wang, Y.; Jiang, F.; Chen, J. In situ construction of CNT/CuS hybrids and their application in photodegradation for removing organic dyes. *Nanomaterials* **2020**, *10*, 178. [[CrossRef](#)]
8. Hong, J.; Kim, B.S.; Hou, B. Room temperature wafer-scale synthesis of highly transparent, conductive CuS nanosheet films via a simple sulfur adsorption-corrosion method. *ACS Appl. Mater. Interfaces* **2021**, *13*, 4244–4252. [[CrossRef](#)]
9. Feng, X.; Chen, W.; Yan, L. Reduced graphene oxide hydrogel film with a continuous ion transport network for supercapacitors. *Nanoscale* **2015**, *7*, 3712–3718. [[CrossRef](#)]
10. Zhao, S.; Li, M.; Wu, X. Graphene-based free-standing bendable films: Designs, fabrications, and applications. *Mater. Today Adv.* **2020**, *6*, 100060. [[CrossRef](#)]
11. Chen, W.P.; Chou, Y.C.; Wang, P.Y. Integration of ultrathin MoS₂/PANI/CNT composite paper in producing all-solid-state flexible supercapacitors with exceptional volumetric energy density. *J. Phys. Chem. C* **2019**, *123*, 17864–17872. [[CrossRef](#)]
12. Liu, C.; Yan, X.; Hu, F.; Gao, G.; Wu, G.; Yang, X. Toward superior capacitive energy storage: Recent advances in pore engineering for dense electrodes. *Adv. Mater.* **2018**, *30*, 1705713. [[CrossRef](#)] [[PubMed](#)]
13. Chen, H.; Zeng, S.; Chen, M.; Zhang, Y.; Li, Q. Fabrication and functionalization of carbon nanotube films for high-performance flexible supercapacitors. *Carbon* **2015**, *92*, 271–296. [[CrossRef](#)]
14. Chen, L.; Li, D.; Chen, L.; Si, P.; Feng, J.; Zhang, L.; Li, Y.; Lou, J.; Ci, L. Core-shell structured carbon nanofibers yarn@polypyrrole@graphene for high performance all-solid-state fiber supercapacitors. *Carbon* **2018**, *138*, 264–270. [[CrossRef](#)]
15. Liu, L.L.; Niu, Z.Q.; Zhang, L. Nanostructured graphene composite papers for highly flexible and foldable supercapacitors. *Adv. Mater.* **2014**, *26*, 4855–4862. [[CrossRef](#)]
16. Xiong, Z.Y.; Liao, C.L.; Han, W.H. Mechanically tough large-area hierarchical porous graphene films for high-performance flexible supercapacitor applications. *Adv. Mater.* **2015**, *27*, 4469–4475. [[CrossRef](#)]
17. Mohan, V.B.; Lau, K.T.; Hui, D. Graphene-based materials and their composites: A review on production, applications and product limitations. *Compos. B. Eng.* **2018**, *142*, 200–220. [[CrossRef](#)]
18. Conway, B.E.; Birss, V.; Wojtowicz, J. The role and utilization of pseudocapacitance for energy storage by supercapacitors. *J. Power Sources* **1997**, *66*, 1–14. [[CrossRef](#)]

19. Wang, Y.M.; Chen, J.C.; Cao, J.Y. Graphene/carbon black hybrid film for flexible and high rate performance supercapacitor. *J. Power Sources* **2014**, *271*, 269–277. [[CrossRef](#)]
20. Borenstein, A.; Hanna, O.; Attias, R. Carbon-based composite materials for supercapacitor electrodes: A review. *J. Mater. Chem. A* **2017**, *5*, 12653–12672. [[CrossRef](#)]
21. Li, Y.W.; Yang, H.X.; Paul, K. Hierarchical CoMoO₄@Co₃O₄ nanocomposites on an ordered macro-porous electrode plate as a multi-dimensional electrode in high-performance supercapacitors. *Mater. Chem. A* **2017**, *5*, 17312–17324. [[CrossRef](#)]
22. Wang, J.G.; Kang, F.Y.; Wei, B.Q. Engineering of MnO₂-based nanocomposites for high-performance supercapacitors. *Prog. Mater. Sci.* **2015**, *74*, 51–124. [[CrossRef](#)]
23. Seyed, N.H.; Chen, X.D.; Patrick, J. Synthesis and characterization of anatase TiO₂ nanorods: Insights from nanorods' formation and self-assembly. *Appl. Sci.* **2022**, *12*, 1614–1619.
24. Gong, Y.M.; Zhao, J.C.; Wang, H.X. CuCo₂S₄/reduced graphene oxide nanocomposites synthesized by one-step solvothermal method as anode materials for sodium ion batteries. *Electrochim. Acta.* **2018**, *292*, 895–902. [[CrossRef](#)]
25. Chi, K.; Zhang, Z.Y.; Lv, Q. Well-ordered oxygen-deficient CoMoO₄ and Fe₂O₃ nanoplate arrays on 3D graphene foam: Toward flexible asymmetric supercapacitors with enhanced capacitive properties. *ACS Appl. Mater. Interfaces* **2017**, *9*, 6044–6053. [[CrossRef](#)]
26. Lai, C.H.; Ashby, D.; Moz, M. Designing pseudocapacitance for Nb₂O₅/carbide-derived carbon electrodes and hybrid devices. *Langmuir* **2017**, *33*, 9407–9415. [[CrossRef](#)]
27. Shown, I.; Ganguly, A.; Chen, L.C. Conducting polymer-based flexible supercapacitor. *Energy Sci. Eng.* **2015**, *3*, 2–26. [[CrossRef](#)]
28. Lv, Z.S.; Luo, Y.F.; Tang, Y.X. Editable supercapacitors with customizable stretchability based on mechanically strengthened ultralong MnO₂ nanowire composite. *Adv. Mater.* **2018**, *30*, 1704531. [[CrossRef](#)]
29. Liu, P.B.; Yan, J.; Guang, Z.X. Recent advancements of polyaniline-based nanocomposites for supercapacitors. *J. Power Sources* **2019**, *424*, 108–130. [[CrossRef](#)]
30. Liu, B.; Kong, D.; Huang, Z.X.; Mo, R.; Wang, Y.; Han, Z.; Cheng, C.; Yang, H.Y. Three-dimensional hierarchical NiCo₂O₄ nanowire@Ni₃S₂ nanosheet core/shell arrays for flexible asymmetric supercapacitors. *Nanoscale* **2016**, *827*, 10686–10694. [[CrossRef](#)]
31. Manickam, M.; Kethaki, W. Electrochemical aspects of supercapacitors in perspective: From electrochemical configurations to electrode materials processing. *J. Solid State Chem.* **2023**, *69*, 100390.
32. Kethaki, W.; Manickam, M. Consequences of electrodeposition parameters on the microstructure and electrochemical behavior of electrolytic manganese dioxide (EMD) for supercapacitor. *Ceram. Int.* **2022**, *14*, 19913–19924.
33. Zhang, C.; Kuila, T.; Kim, N.H.; Lee, S.H.; Lee, J.H. Facile preparation of flower-like NiCo₂O₄/three dimensional graphene foam hybrid for high performance supercapacitor electrodes. *Carbon* **2015**, *89*, 328–339. [[CrossRef](#)]
34. Yang, S.; Han, Z.; Zheng, F.; Sun, J.; Qiao, Z.; Yang, X.; Li, L.; Li, C.; Song, X.; Cao, B. ZnFe₂O₄ nanoparticles-cotton derived hierarchical porous active carbon fibers for high rate-capability supercapacitor electrodes. *Carbon* **2018**, *134*, 15–21. [[CrossRef](#)]

Disclaimer/Publisher's Note: The statements, opinions and data contained in all publications are solely those of the individual author(s) and contributor(s) and not of MDPI and/or the editor(s). MDPI and/or the editor(s) disclaim responsibility for any injury to people or property resulting from any ideas, methods, instructions or products referred to in the content.